

## Article

# Design and Modeling of Viscoelastic Layers for Locomotive Wheel Damping

Mpho Podile <sup>1,\*</sup>, Daramy Vandi Von Kallon <sup>1</sup> , Bingo Masiza Balekwa <sup>1</sup> and Michele Cali <sup>2</sup> 

<sup>1</sup> Department of Mechanical and Industrial Engineering Technology, University of Johannesburg, Level 7, John Orr Building, 47 Nind Street, Doornfontein, Johannesburg 2092, South Africa; dkallon@uj.ac.za (D.V.V.K.); bingo.balekwa@transnet.net (B.M.B.)

<sup>2</sup> Electric, Electronics and Computer Engineering Department, University of Catania, 95125 Catania, Italy; michele.cali@unict.it

\* Correspondence: 201210147@student.uj.ac.za; Tel.: +27-71-913-4031

**Abstract:** Rail–wheel interaction is one of the most significant and studied aspects of rail vehicle dynamics. The vibrations caused by rail–wheel interaction can become critical when the radial, lateral and longitudinal loads of the vehicle, cargo and passengers are experienced while the vehicle is in motion along winding railroad paths. This mainly causes an excessive production of vibrations that may lead to discomfort for the passengers and shortening of the life span of the vehicle’s body parts. The use of harmonic response analysis (HRA) shows that the wheel experiences high vibrational amplitudes from both radial and lateral excitation. The present study describes a numerical and experimental design procedure that allows mitigation of the locomotive wheel resonance during radial and lateral excitations through viscoelastic layers. It is proven that these high frequencies can be reduced through the proper design of damping layer mechanisms. In particular, three parametric viscoelastic damping layer arrangements were analyzed (on the web of both wheel sides, under the rim of both wheel sides and on the web and under the rim of both wheel sides). The results demonstrate that the correct design and dimensions of these viscoelastic damping layers reduce the high-amplitude resonance peaks of the wheel successfully during both radial and lateral excitation.

**Keywords:** modal analysis; web and rim parametric design; harmonic response analysis; viscoelastic damping layers; radial excitation; lateral excitation



**Citation:** Podile, M.; Kallon, D.V.V.; Balekwa, B.M.; Cali, M. Design and Modeling of Viscoelastic Layers for Locomotive Wheel Damping. *Vibration* **2021**, *4*, 906–937. <https://doi.org/10.3390/vibration4040051>

Academic Editor: Zuzana Dimitrovová

Received: 25 September 2021  
Accepted: 8 December 2021  
Published: 16 December 2021

**Publisher’s Note:** MDPI stays neutral with regard to jurisdictional claims in published maps and institutional affiliations.



**Copyright:** © 2021 by the authors. Licensee MDPI, Basel, Switzerland. This article is an open access article distributed under the terms and conditions of the Creative Commons Attribution (CC BY) license (<https://creativecommons.org/licenses/by/4.0/>).

## 1. Introduction

The wheel–rail contact dynamics of trains in motion are a complex phenomenon that requires in-depth analysis. Currently, this analysis is expressed by numerical modeling in some available commercial software with the computational ability to analyze complex problems. For instance, Thomson utilized a 2D model to examine the transient vibration characteristics of a train wheel [1]. Sato et al. [2] investigated the vibration and sound radiation characteristics of rail wheels by conducting experiments and validating their results through modeling the wheel and performing Finite Element Analysis (FEA). Zhong et al. [3] studied the vibration and sound radiation of a rotating train wheel subjected to vertical harmonic wheel–rail force (with and without rotation) using 2.5DFinite Element Method (FEM) to calculate the wheel vibration characteristics and validating their findings with the experimental results. They concluded that the wheel rotation speed splits most peaks of the vertical receptance at the wheel–rail contact point [4]. Mazilu [5] examined the radial and axial wheel vibration by using both theoretical and experimental approaches and concluded that larger resonance peaks of frequencies at radial excitation would start at frequencies larger than 1500 Hz. It was also observed that radial excitation would experience higher amplitude resonance peaks than lateral excitation.

It is known that vibrations in rails are caused by vehicle force on the railroad tracks from the wheels and from irregularities at the wheel–rail interference (corrugation). As

a prevalent consequence, rail–wheel vibration can result in rolling noise, shorten the life cycle of the rolling surfaces from wear or cause discomfort to passengers, tonal noise and damage to the vehicle’s structural components. Additionally, excessive vibration on a rail wheel has long been acknowledged to be caused by rail wheel corrugation [3–7]. Balekwa and Kallon [8] investigated resonance frequencies via experimental and Finite Element Modal Analysis (FEMA) of the class D39 200 locomotive wheelset, correlating their results with corrugation frequencies around the track curves [9]. The locomotive class D39 200 is normally operated on the Belfast to Steelpoort railway line. This study highlighted how the locomotive experiences rail corrugation when passing through track curves, resulting in excessive rail wheel vibrations [10–12].

The main focus of the present manuscript was to develop a design procedure that allowed for mitigating locomotive wheel resonance during radial and lateral excitations through parametric modeling of viscoelastic layers. The originality of the study lies in the optimization method adopted. Through the application of computational methods and the experimental characterization of the damping, this allowed for finding the optimal geometry of the layers that minimized wheel vibrations in a wide range of frequencies.

In short, three viscoelastic damping layers were parametrically designed to be mounted on the locomotive wheel structure, being in contact at a point where the structure experiences high deformation in such a way that the viscoelastic damping layer cannot but dissipate energy as much as possible.

A case study of the locomotive class D39 200 wheel offered tangible results to support the methodology by validating it with experimental data. The resonance amplitude peaks observed in the wheels of this locomotive [8–13] were damped using this new viscoelastic passive damping design technique.

To be precise, the viscoelastic damping layer, which is applied on structures to mitigate vibrations, can be either an unconstrained (free) damping layer or a constrained damping layer. The difference is that a constrained damping layer consists of a steel or aluminum layer with a viscoelastic high-damping polymer sheet mounted between the structure and steel, while an unconstrained (free) damping layer is used instead when the viscoelastic high-damping polymer is mounted on the structure [14–16]. It is clear that the advantages of viscoelastic damping can be identified in the material properties, which consist of elastic and viscous characteristics at the same time.

Lopez [17] studied a wheel fitted with a steel rod ring inside the groove cut under the rim. The motion between the wheel and ring reduced vibration gradually through friction and interference by converting the vibration into heat. The conclusion was that by also increasing the ring damper mass mounted on the wheel, the damping efficiency on the wheel increased. The problem is that the theoretical design mechanism of this type of damping procedure, called a ring damper, is still not well understood [18]. As an advantage, ring dampers are simple and cost-effective compared with other wheel dampers. Figure 1 shows the rail wheel mounted with a damping ring under the rim of both sides of the wheel [19].



**Figure 1.** Damping ring under the rim of both sides of the wheel [19].

It should be noted that many researchers have investigated tuned mass dampers (TMDs) for different applications like rail wheels, beams and railway bridges [20–22]. A TMD, first developed by Frahm in 1909 [23,24], is a device having a mass–spring–damper system integral to the structure to reduce the dynamic response. Later in his book on mechanical vibrations, Den Hartog used a tuned mass damper to mitigate vibrations in systems [25]. The frequency of the damper is tuned to a structural frequency so that during excitation, the TMD resonates out of phase with the structural motion, reducing unwanted energy depending on the modal displacement in the system. The mass damper consists of a viscous elastic layer which can turn the vibration into heat energy [26] (Figure 2).



**Figure 2.** Locomotive wheel with tuned mass damper [26].

Suarez et al. [27] compared the vibration and noise of resilient and solid monobloc railway wheels on underground lines. Based on their results, the resilient wheels demonstrated better performance. It is the resilient wheel which is commonly designed for light transit systems in order to mitigate the dynamic vibration of the wheel, rolling noise produced by wheel–rail contact and wheel squeal noise on sharp curves [28] (Figure 3).



**Figure 3.** Locomotive wheel with resilient layer inserted between the hub and tread [28].

In light of these considerations, in the present study, the viscoelastic damping layer material 3M ISD112 [29] was chosen because of its widespread use and commercial availability [30–33].

Introduction excluded, the manuscript is organized into four sections. In the first section, the experimental and numerical analysis methodology are illustrated. In the second section, the principal results obtained for different viscoelastic layer positions and arrangements are discussed. The final considerations and conclusions are discussed in sections three and four, respectively.

## 2. Materials and Methods

The dynamic characterization of the D39 200 locomotive wheel and the design of the viscoelastic layers to damp wheel vibrations were performed by means of numerical analysis validated through experimental modal analysis (EMA). EMA was carried out by a roving hammer impact test with a Brüel & Kjær piezoelectric charge hammer (Brüel & Kjær, Nærum, Denmark) and a small-sized charge accelerometer (Figure 4). Frontend data and

the specific software Test Xpress Version 10.0 and TestLab Version 16 from Siemens/LMS (Plano, TX, USA) were used for the acquisition of signals, post-processing, FRF calculations and complete identification of the main modes [34].



**Figure 4.** Experimental modal analysis (EMA) of D39200 locomotive wheel.

Here, the results of the EMA allowed us to fine-tune and validate a nonlinear finite element (FE) model of the wheel with energy absorption capabilities. Harmonic response analyses with the FE model of the wheel were performed through radial and lateral excitations, with the wheel assumed to be rigidly mounted on the axle. Viscoelastic damping layers were introduced into the FE model in three different arrangements of the wheel, and an optimization of vibration amplitude reduction was performed.

### 2.1. Finite Element Modal Analysis

The FE model of the locomotive wheel was meshed using 54,496 nodes and 32,606 tetrahedral 10-node elements (SOLID187) to determine the frequency at which the wheel would experience high-amplitude oscillations that could lead to resonance. The characteristics of the wheel, as well as the finite element modal and harmonic analysis, were performed with ANSYS 2020 R1 (ANSYS Inc., Canonsburg, PA, USA) software (Figure 5).

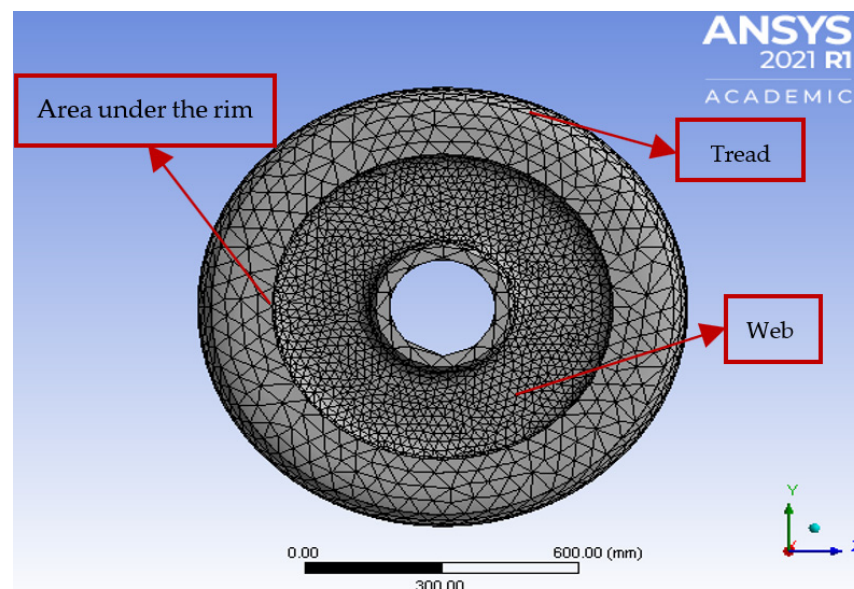


**Figure 5.** Finite element model of D39200 locomotive wheel.

The wheel's geometric profile, containing curves on the web and under the rim, makes tetrahedron mesh elements particularly suitable to fit the wheel's geometry [35]. Thus,

using Autodesk Inventor code a parametrization of the wheel and damping layer profile was carried out. This process provided the parametric geometric profiles of the cross sections of the three types of layers (on the web of both wheel sides, under the rim of both wheel sides and on the web and under the rim of both wheel sides) used to dampen the vibrations of the wheel (Figure 6a).

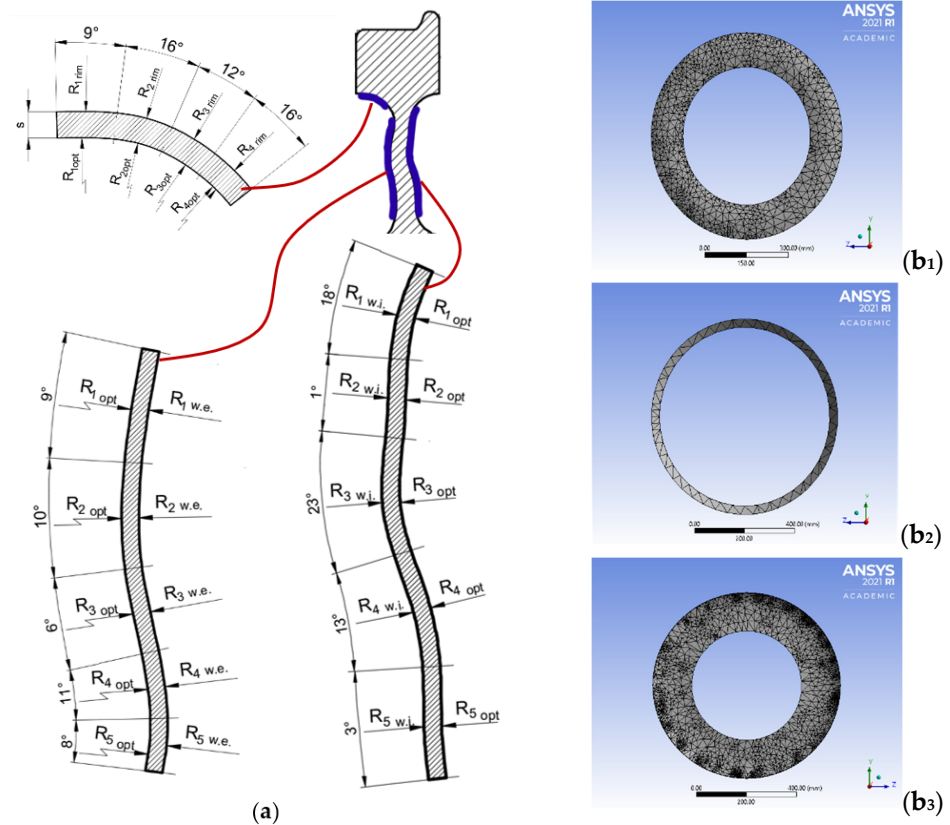


**Figure 6.** Viscoelastic damping layers. (a) Profile parametrization. (b<sub>1</sub>–b<sub>3</sub>) FE models.

The initial values of the geometric parameters of the layers' section profiles were obtained by approximating the profiles both under the rim and for the web of both wheel sides with polycentric curves. In particular, four circular arcs were used to approximate the section profile of the under the rim layer, and five circular arcs were used to approximate the section profile on the web of both wheel sides with an accuracy of over 99%. The values of the radii of these arcs constituted the design variables for optimization (Figure 6a).

After the mesh refinement procedure, which allowed us to validate the FE model based on the EMA, the best geometry of the layers and their best arrangement, which gave the optimal results in terms of vibration damping in the frequency range studied, were calculated. The design values, the optimal values assigned to the radii (design variables) in the parametric optimization study carried out, are shown in Table 1. The optimal values adopted for the radii of the profiles are the best compromise between the maximum allowed values (Table 1) and the space requirements of the wheel. They provided optimal thickness values of 8 mm and 10 mm for the viscoelastic damping layer under the rim and the viscoelastic damping layer, respectively.

**Table 1.** Layer profile geometric parameters.

Parameter	R <sub>1rim</sub>	R <sub>2rim</sub>	R <sub>3rim</sub>	R <sub>4rim</sub>	R <sub>1w.i.</sub>	R <sub>2w.i.</sub>	R <sub>3w.i.</sub>	R <sub>4w.i.</sub>	R <sub>5w.i.</sub>	R <sub>1w.e.</sub>	R <sub>2w.e.</sub>	R <sub>3w.e.</sub>	R <sub>4w.e.</sub>	R <sub>5w.e.</sub>
On design values	72.1	54.5	62.3	67.4	167.2	223.6	173.4	216.8	289.4	423.4	216.8	354.7	189.2	102.7
Max. variation	12	12	12	12	16	16	16	16	16	14	14	14	14	14
Optimal values	64.1	46.5	54.3	59.4	157.2	213.6	163.4	206.8	279.4	413.4	206.8	344.7	179.2	92.7

Figure 6b shows the mesh of the three optimal viscoelastic layer arrangements. The internal web viscoelastic damping layer was meshed using 14,710 nodes and 4459 tetrahedron elements (Figure 6b<sub>1</sub>). The viscoelastic damping layer under the rim was meshed using 7025 nodes and 2778 tetrahedron elements (Figure 6b<sub>2</sub>). The external web viscoelastic damping layer was meshed using 12,025 nodes and 3781 tetrahedron elements (Figure 6b<sub>3</sub>). The mesh size for all three configurations of viscoelastic damping layers was 2 mm.

The mesh refinement procedure was performed by setting 5% as the maximum admissible limit of frequency variation with respect to the values calculated through EMA. Mesh convergence was measured on the sixth deformation mode only for all mesh sizes. Mesh convergence is a good tool to verify if the mesh results are adequate, since the accuracy of a simulation depends on the geometry accuracy, material properties and loads and boundary conditions.

Evident from Table 2 is that the results did not change with continued mesh refinement. Hence, it can be deduced that convergence was reached using 54,496 nodes and 32,606 tetrahedral elements. Table 3 shows the material properties adopted in the FE analysis.

**Table 2.** Mesh convergence.

Frequency (Hz)	Frequency Variation	Nodes	Elements
543.31	Experimental value	-	-
540.75	-0.47	4214	1531
541.56	-0.32	8672	4531
541.83	-0.27	54,496	32,606
541.05	-0.41	65,395	39,127

**Table 3.** Material properties of the FEA model.

Material	Young's Modulus (GPa)	Density (kg/m <sup>3</sup> )	Poisson's Ratio
Steel	210	7850	0.3

## 2.2. Harmonic Response Analysis

Harmonic Response Analysis (HRA) was conducted from 20 Hz to 5 kHz at 20-Hz intervals. The wheel was set free radially ( $y$ -axis) and laterally ( $x$ -axis). Two directions of the wheel, radial (vertically), and lateral (axially), were excited by a unitary force to investigate the frequency which would experience maximum amplitudes, leading to resonance of the locomotive wheel [36]. Figure 6a shows the wheel model with the load being applied radially (Figure 7a). Hence, the impact would represent the vertical harmonic wheel-rail force at the wheel-rail contact point. Figure 7b shows the load being applied laterally on the wheel model instead. The lateral impact represents the axial harmonic wheel-rail instability that results when the wheel travels through sharp curves while the wheel is experiencing lateral creepage impacts.

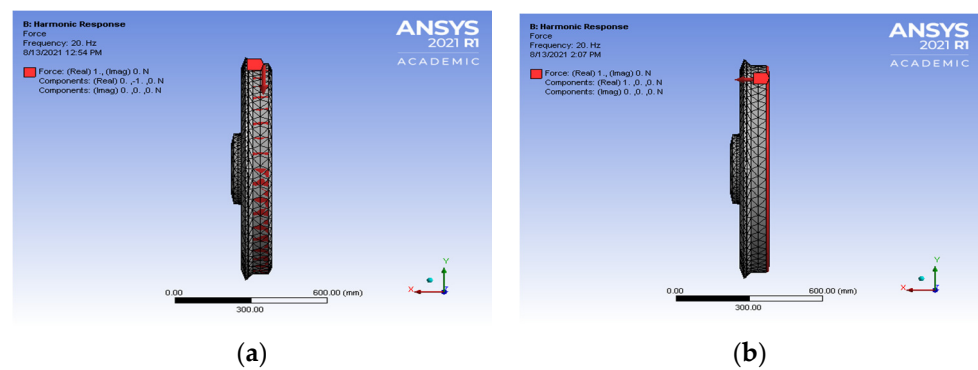


**Figure 7.** Finite element model of the wheel: (a) radial excitation and (b) lateral excitation.

### 2.3. Viscoelastic Damping Layers

Viscoelastic materials have very effective characteristics for controlling vibrations in structural systems. The use of a viscoelastic damping layer depends on the material properties [37,38]. The viscoelastic material considered in this research was 3M ISD112 from the 3M™ Viscoelastic Damping Polymers manufacturing company (Tokyo, Japan) because of its widespread use and its commercial availability [31–33]. However, the procedure utilized in the scientific literature can obviously be applied to any viscoelastic material. The properties of the viscoelastic material studied in this paper were approximated by the elastic properties listed in Table 4, and viscous damping would be added additionally by Rayleigh beta damping. ANSYS was adopted to investigate the harmonic response of the wheel, with a viscoelastic damping layer mounted in the three different arrangements shown in Figure 6a–c.

**Table 4.** The viscoelastic layer’s material properties.

Material Type	Young’s Modulus (E)	Density ( $\rho$ )	Poisson’s Ratio	Shear Modulus (G)
Viscoelastic material 3M ISD 112	$833.78 \times 10^4 \text{ N/m}^2$	$1350 \text{ kg/m}^3$	0.49	$277.93 \times 10^4 \text{ N/m}^2$

It was assumed that the viscoelastic damping material only underwent small deformations and hence had linear behavior. The element type used to characterize the viscoelastic damping layer material was the same used in the wheel model in order to ensure good boundary definition. It was proven by Pascon et al. [39] that the use of tetrahedral elements to solve problems with high polymetric layer materials using Finite Element Analysis does not present locking nor results making the layer too stiff, even if the material layer is applied with other different materials inside the analyzed domain.

For the viscoelastic layers in three optimal configurations, FEMA and HRA of the wheel were performed, and the natural frequencies for the three different positions (Figure 8a–c) were calculated.

The viscoelastic damping layer was mounted with a strong bonding agent to be in contact with the vibrating structural surface (Figure 9c). During the vibration of a structure, the viscoelastic damping layer material dissipates vibrations by means of alternate extension and compression of the viscoelastic damping layer as demonstrated in Figure 9a,b.

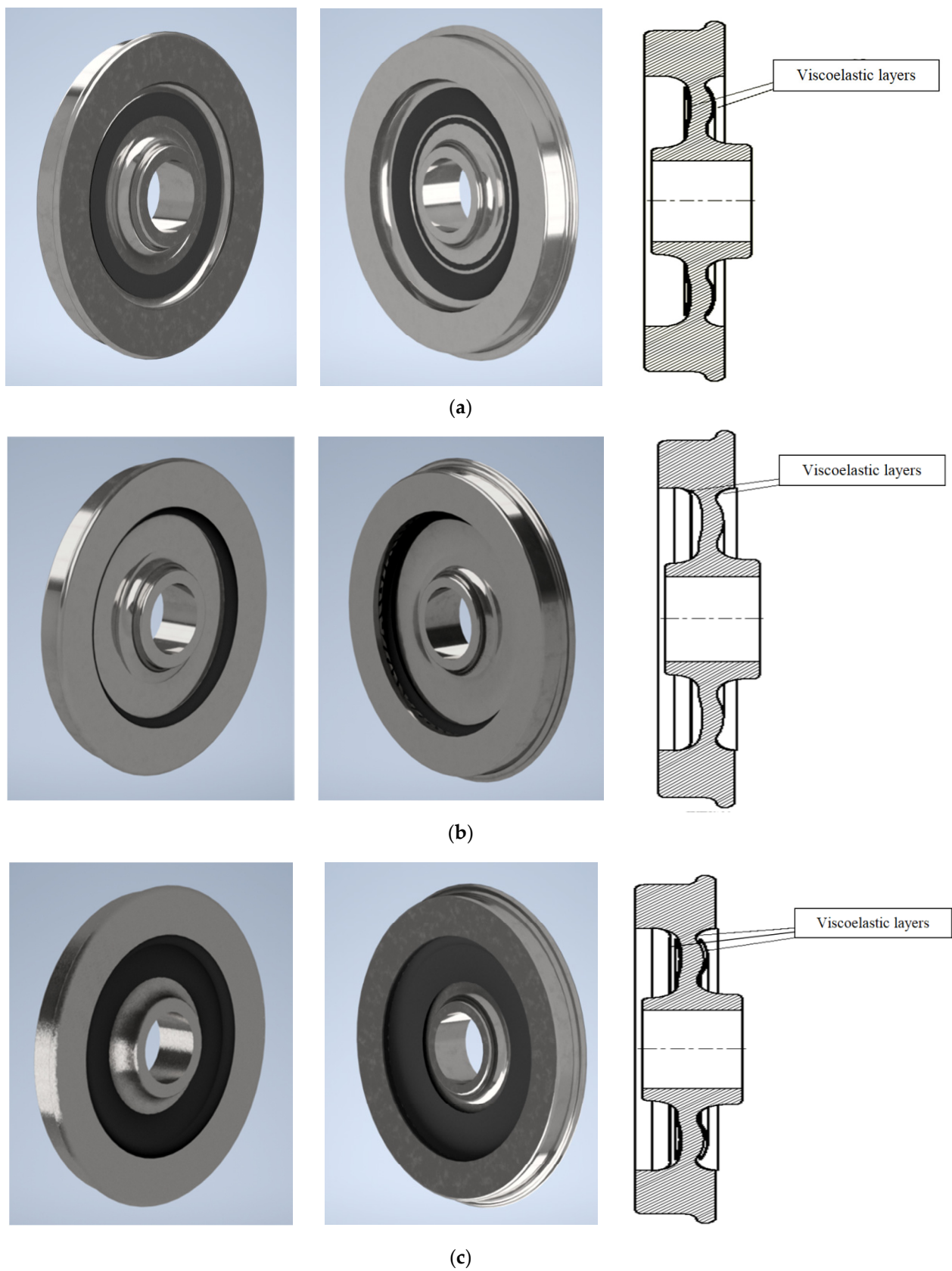


**Figure 8.** (a) Viscoelastic layer on the webs. (b) Viscoelastic layer under the rim. (c) Viscoelastic layer on the webs and under the rim.

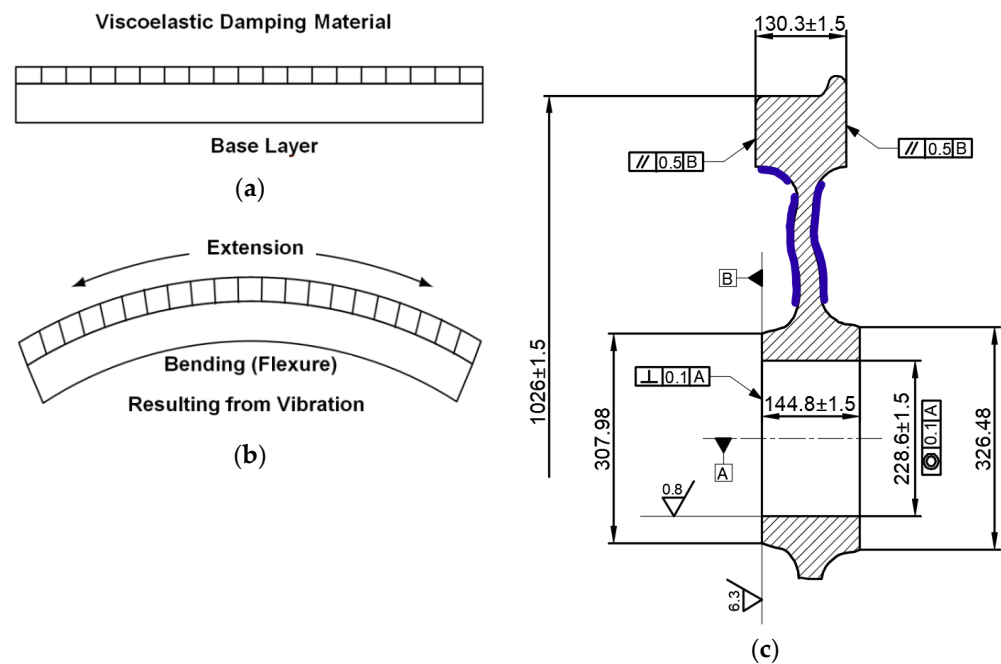


**Figure 9.** (a) Base structure of the viscoelastic damping layer. (b) Changing of extension and compression of the viscoelastic damping layer. (c) Final executive drawings of the D39 200 locomotive wheel.

The mesh convergence was conducted by decreasing the element size for the viscoelastic damping layers of the web and under the rim. The viscoelastic damping layers on the web and under the rim were chosen to track the convergence since they consisted of both web and under the rim damping components. Table 5 shows the details of the convergence results of the viscoelastic damping layer.

**Table 5.** Mesh convergence of damping layers on the web and under the rim.

Deformation (mm)	Variation	Nodes	Elements
54.182	-	12,025	3781
54.191	0.13611	64,432	21,037

Figure 9c and Table 6 show the final optimized model of the wheel for a class D39 200 locomotive and its design dimensions, respectively.

**Table 6.** Wheel design dimensions.

Description	Metric Value (mm)	Description	Metric Value (mm)
Wheel diameter	1026	Front of hub diameter	317.5
Rim thickness	104.8	Back of hub diameter	336.6
New wheel diameter	104.8	Bore diameter	228.6
Hub offset	18	Plate thickness at rim	25.4
Back of rim to front of hub	130.3	Plate thickness at hub	30.2
Hub length	148.3		
Rim width	141		

*2.4. Harmonic Excitation of a Wheel with Viscoelastic Damping Layers*

Finally, the boundary conditions of the wheel were set free radially (*y*-axis) and laterally (*x*-axis). Two directions of the wheel, radial and lateral, were excited by unitary force.

### 3. Results

The results are outlined in the following order: FEA modal analysis of the wheelset and the Harmonic Response Analysis of the wheel with and without viscoelastic damping layers.

#### 3.1. Finite Element Modal Analysis

Table 7 shows the results obtained with FE modal analysis. The mode of vibrations that were relevant to the lateral mode were identified due to out-of-plane displacement of the web [40]. The legends illustrate the displacements in millimeters. It was noted from the fourth mode, for example, that the nodes of the wheel situated around the light blue color code of the deformed shape displaced the least (about 0.36743 mm). The nodes situated around the green and yellow color codes experienced an average displacement of 2.1252 mm, while the modes around the orange and red color codes experienced a larger displacement of 3.3069 mm. The second and third modes had no complex mode shape, but from the fourth mode, the shape of the wheel started to deform to different eigenmodes. Finite element modal and harmonic analysis of the wheel mounted with viscoelastic damping layer were performed, and the first 20 natural frequencies for 3 different positions are outlined in Appendix A, Appendix B, Appendix C, Appendix D. Table 7 shows the first seven natural frequencies and the relative mode shapes.

Table 7. First natural frequencies of the wheel.

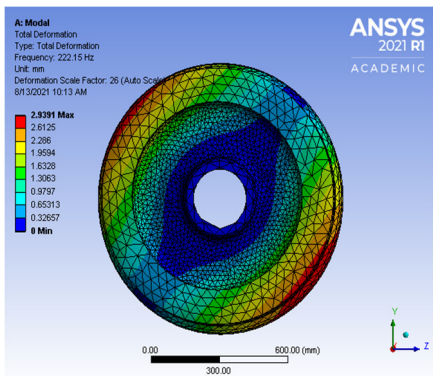
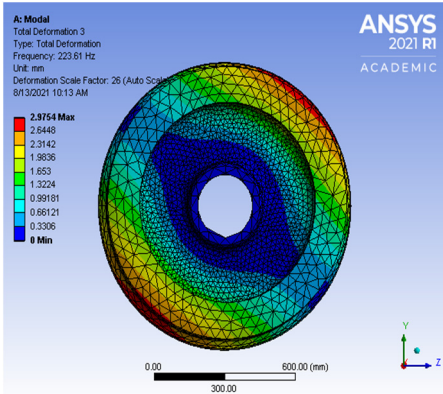
Mode Number	Frequency (Hz)	Mode Shapes	Classification and Descriptions
1	222.15		Lateral Mode: High deformation at the wheel flange and rim.
2	223.61		Lateral Mode: Bending of the web.

Table 7. Cont.

Mode Number	Frequency (Hz)	Mode Shapes	Classification and Descriptions
3	302.9		Lateral Mode: High deformation at the wheel flange and rim.
4	459.92		Lateral Mode: Larger deformed area on the wheel flange.
5	460.91		Radial Mode: Cross-section of the wheel starts to alter.
6	543.31		Lateral Mode: Wheel flange and rim are laterally twisted.

Table 7. Cont.

Mode Number	Frequency (Hz)	Mode Shapes	Classification and Descriptions
7	1137		Radial Mode: Larger deformations on the rim, flange and under the rim.

The radial modes were easily identified by observing the axial bending vibrations of the wheel. The nodes situated around the green and yellow colors experienced, on average, the smallest displacement, while the modes around the orange and red colors experienced larger displacements.

### 3.2. Harmonic Response Analysis of a Wheel without Viscoelastic Damping Layers

#### 3.2.1. Lateral Harmonic Response of the Wheel

Figure 10 shows the behavior of the wheel’s lateral harmonic response.

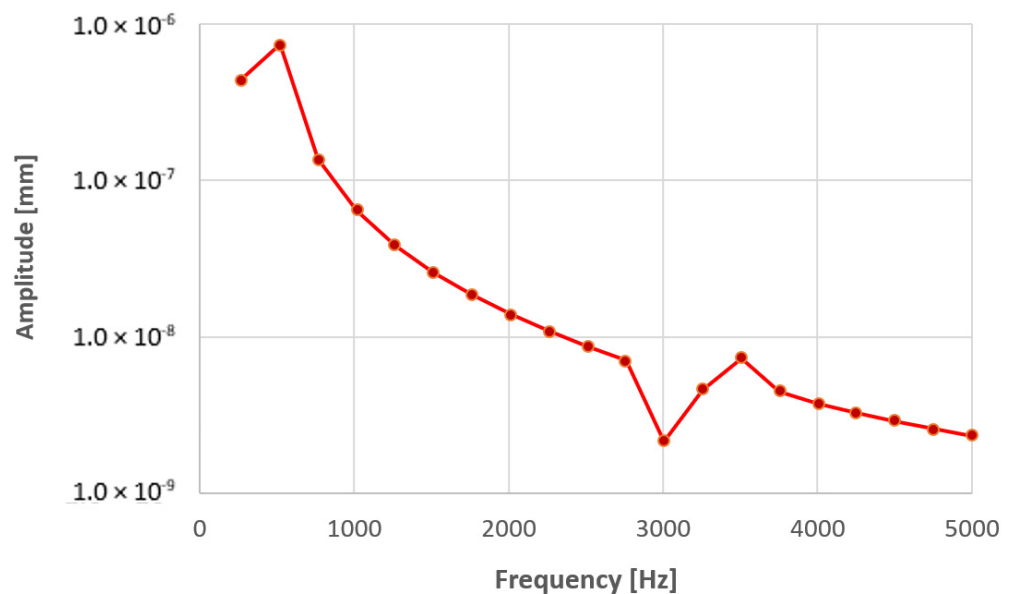


Figure 10. Lateral harmonic response of the wheel.

The *x*-axis of the graph represents the frequencies, while the *y*-axis represents the amplitudes in terms of the normalized amplitude (mm/N). Figure 10 illustrates the lateral harmonic response results. The wheel structure had a maximum amplitude of  $741.669 \times 10^{-9}$  mm at a frequency of 518 Hz.

#### 3.2.2. Radial Harmonic Response of the Wheel

Figure 11 shows the wheel’s radial harmonic response. The wheel structure had a maximum amplitude of  $640.024 \times 10^{-9}$  mm at a frequency of 1265 Hz. It was evident from the harmonic response results in the radial and lateral frequency responses that the

wheel vibrated at different amplitudes and frequencies, so it can be deduced that the wheel experienced high amplitudes in the lateral direction. Moreover, the results from Figure 12 reveal that the wheel would reach a maximum radial amplitude of  $640.24 \times 10^{-9}$  mm at a frequency of 1265 Hz. However, during lateral excitation, it would reach a maximum amplitude peak of  $741.669 \times 10^{-9}$  mm at a frequency of 518 Hz.

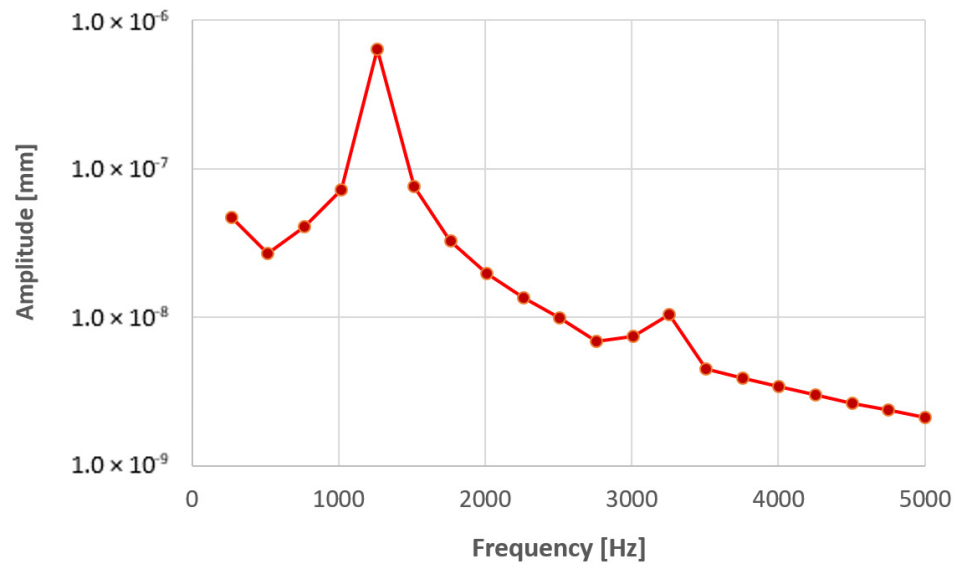


Figure 11. Radial harmonic response of the wheel.

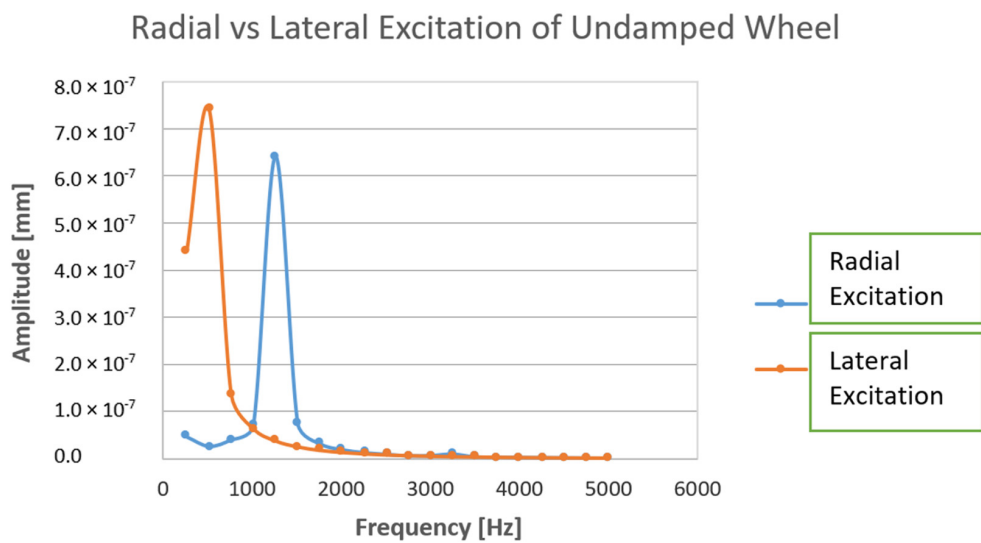


Figure 12. Comparison of the radial and lateral harmonic responses of the wheel.

### 3.2.3. Viscoelastic Material Property Estimation

The final step was to predict the characteristics of the viscoelastic material behavior, whereby the loss factor and modulus of the viscoelastic materials were determined using the modal frequency data of the wheel from Table 8. The procedure was carried out using curve-fitting of the 3M ISD112 viscoelastic material master curve provided by the manufacturer data at 30 °C in the frequency range from 20 Hz to 5 kHz.

**Table 8.** Wheel complex natural frequencies, shear storage modulus and loss factor.

Mode Number	Complex Frequencies (Hz)	Complex Shear Storage Modulus (MPa)	Complex Loss Factor ( $\eta$ )
1	222.15	10.20	0.078
2	223.61	10.03	0.082
3	302.91	11.02	0.091
4	459.92	10.50	0.120
5	460.91	10.31	0.170
6	543.31	10.11	0.198
7	1137.01	1.90	0.355
8	1137.20	1.89	0.356
9	1223.40	1.91	0.361
10	1224.72	1.91	0.362
11	1769.63	1.95	0.372
12	1847.82	1.92	0.377
13	1848.54	1.92	0.378
14	2032.72	1.88	0.389
15	2038.20	1.88	0.390
16	2163.21	1.80	0.401
17	2169.22	1.80	0.403
18	2575.42	1.85	0.434
19	2578.02	1.84	0.436
20	2939.02	1.82	0.501

As it was reported in [29,41], these procedures of determining the viscoelastic material using the master curves provided by manufacturer minimized the difference between the experimental measured and estimated data (Figure 13).

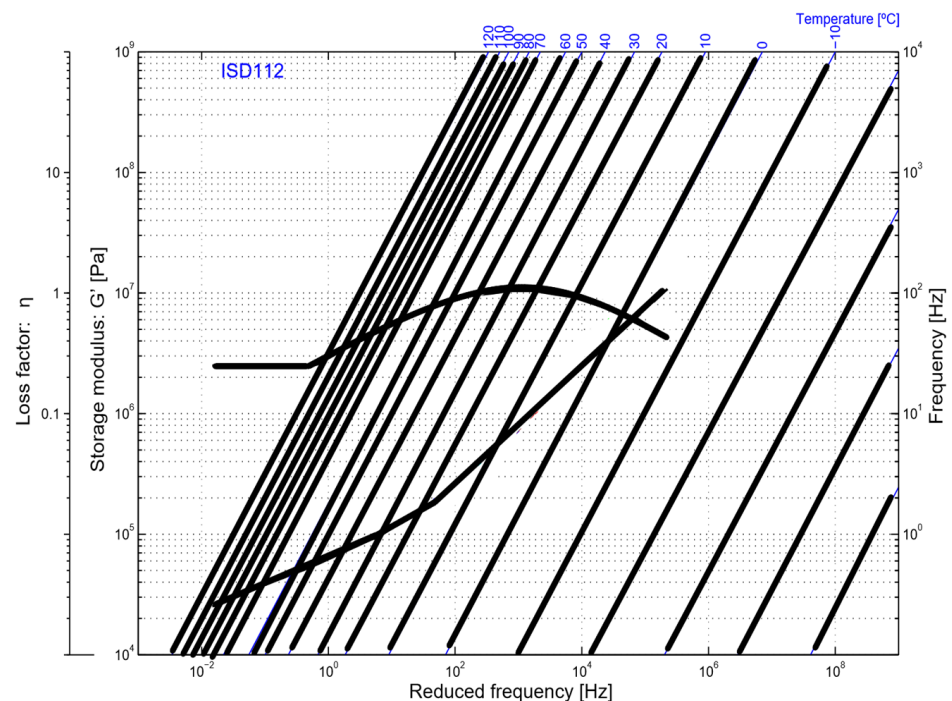


**Figure 13.** Frequency nomograph used to determine the storage modulus and loss factor in the viscoelastic material.

In our application, the primary task was to measure the storage modulus and loss factor of the 3M ISD112 viscoelastic material at the dominating vibrational frequency resonances, as it was indicated that viscoelastic material properties strongly depended on the frequency and temperature [42]. Moreover, the temperature and natural frequency ranges were employed with the nomograph provided by manufacturer of the 3M ISD112 to determine the viscoelastic material behavior of the performance (complex high loss factor

and storage modulus) over the temperature and frequency range of the application [29]. The natural frequency, mode shape and modal masses were assumed to be affected little by the addition of the damping layers, and consequently, the finite element model for the undamped structure was used to derive these parameters [13]. The complex modal analysis was determined using the natural frequencies and the mode shapes of the wheel from Table 7 and were used to predict the modal damping of the complete structure. The procedure's combinations of temperatures and frequencies are depicted in Figure 13. As an example, the natural frequency was found to be 518 Hz (at the modal analyses section), and the temperature was 30 °C (which was assumed to be constant). The point for 518 Hz was found on the right-hand axis. Following the point horizontally to the line for a temperature of 30 °C. At this intersection, the line was drawn to be a vertical line. Then, the modulus and loss factor values were read off the appropriate graph at the point of intersection with the vertical line. The complex storage modulus and loss factor were found to be 10.1 MPa and 0.198, respectively.

Hence, Table 8 demonstrates the numerical loss factor, storage modulus and shear modulus, which were calculated using the nomograph in Figure 13 with the natural frequencies of the locomotive rail wheel that were examined from Appendices A–D. In Appendix E, instead, there is the workflow the procedure followed to design viscoelastic layers.

The rail wheel's equation of motion was

$$[M]\{\ddot{u}\} + [C]\{\dot{u}\} + [K]\{u\} = \{F\} \quad (1)$$

where  $[M]$  and  $[K]$  are the mass and stiffness matrices of the given element, respectively, and  $\{F\}$  is the load vector acting on the element, while  $[C]$  is the damping matrix having the following general form:

$$[C] = \alpha[M] + \beta[K] \quad (2)$$

The equation for the damping ratio is given by two Rayleigh coefficients:

$$\zeta = \frac{\eta}{2} \quad (3)$$

where  $\eta$  is the complex loss factor,  $\zeta$  is the damping ratio,  $\alpha$  is the Rayleigh mass damping coefficient and  $\beta$  is the Rayleigh stiffness damping coefficient. The Rayleigh stiffness damping coefficient was applied and introduced directly in the material properties differently for each material.

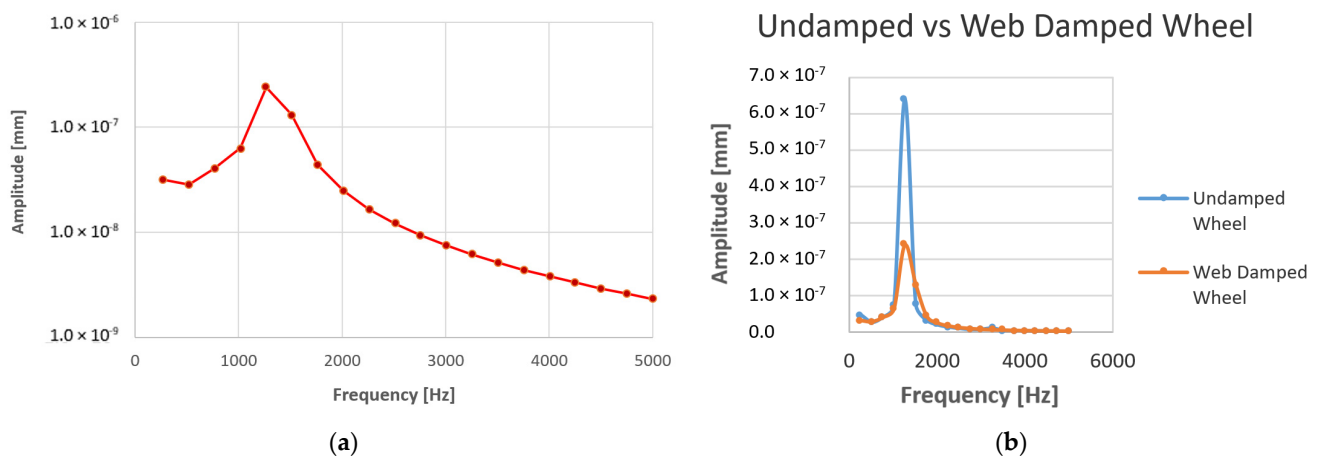
The Rayleigh coefficients were determined using the complex natural frequencies [43]. In this study, the dominating vibrating frequencies with the high amplitude resonance peaks, which were 1265 Hz in the radial excitation from Figure 11 and 518 Hz for the lateral excitation from Figure 10, were used to determine the damping ratio and Rayleigh damping coefficients. However, the Rayleigh mass damping coefficient was neglected to avoid an error drag effect on the wheel.

### 3.3. Harmonic Response Analysis of Wheel with Viscoelastic Damping Layers

#### 3.3.1. Radial Harmonic Analysis of a Wheel Mounted with Viscoelastic Layer on the Web of Both Sides of the Wheel

Figure 14 shows the differences of the wheel without viscoelastic layer (undamped wheel) and with the wheel mounted with viscoelastic layer on the web (damped wheel).

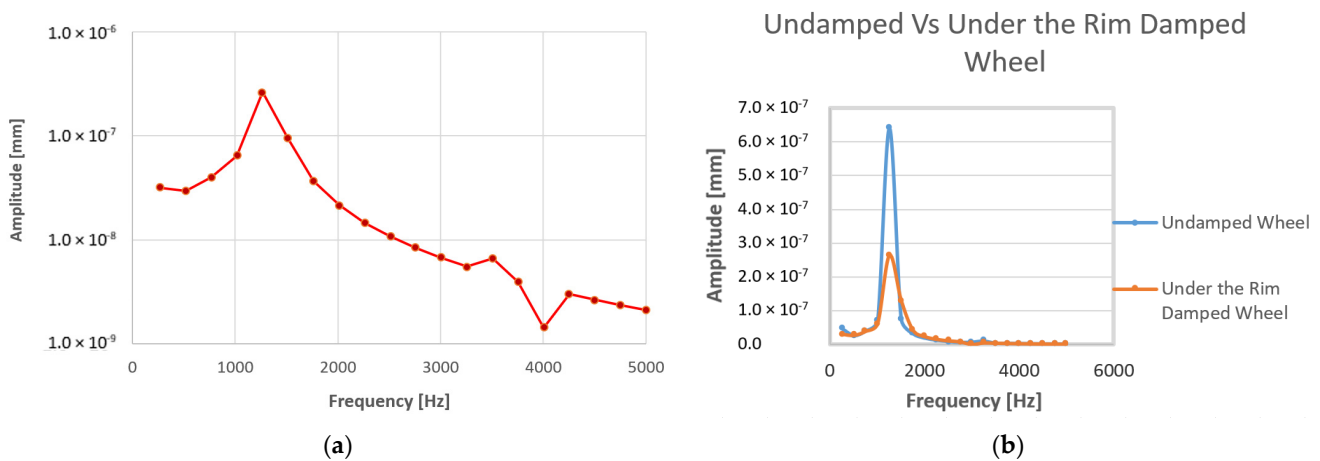
Figure 14b clearly demonstrates that the undamped maximum amplitude peak was  $640.24 \times 10^{-9}$  mm at a frequency of 1265 Hz, and with viscoelastic damping layer on the web, the amplitude was reduced to  $239.54 \times 10^{-9}$  mm at a frequency of 1265 Hz.



**Figure 14.** Harmonic response analysis in the radial direction with viscoelastic damping layer on the web of both sides of the wheel. (a) Radial excitation of the wheel mounted with viscoelastic layer on the web. (b) Comparison between the undamped and web damped wheels when radially excited.

### 3.3.2. Radial Harmonic Analysis of a Wheel Mounted with Viscoelastic Layer on Both Sides under the Rim

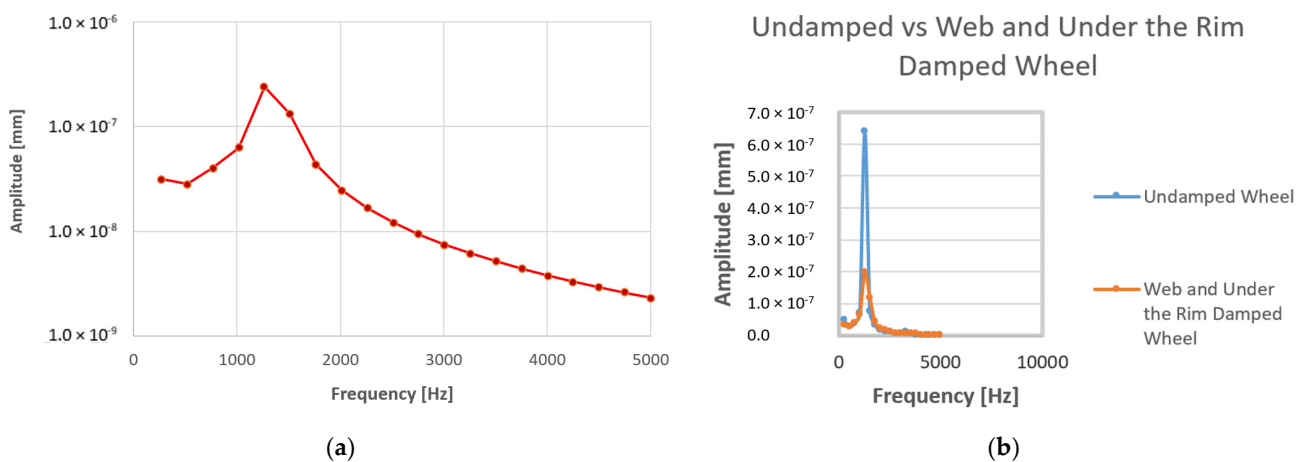
Figure 15 demonstrates the difference between the wheel without viscoelastic layer (undamped wheel) and with the wheel mounted with viscoelastic layer (damped wheel) under the rim on both sides of the wheel. Figure 15b clearly demonstrates that the undamped maximum amplitude peak was  $640.24 \times 10^{-9}$  mm at a frequency of 1265 Hz, and after the viscoelastic damping layer was mounted under the rim on both sides of the wheel, the amplitude was reduced to  $264.4 \times 10^{-9}$  mm at a frequency of 1265 Hz.



**Figure 15.** Harmonic response analysis in the radial direction with viscoelastic damping layer on both sides under the rim. (a) Radial harmonic excitation of the wheel mounted with viscoelastic layer under the rim on both sides of the wheel. (b) Comparison between the undamped and damped wheels when radially excited.

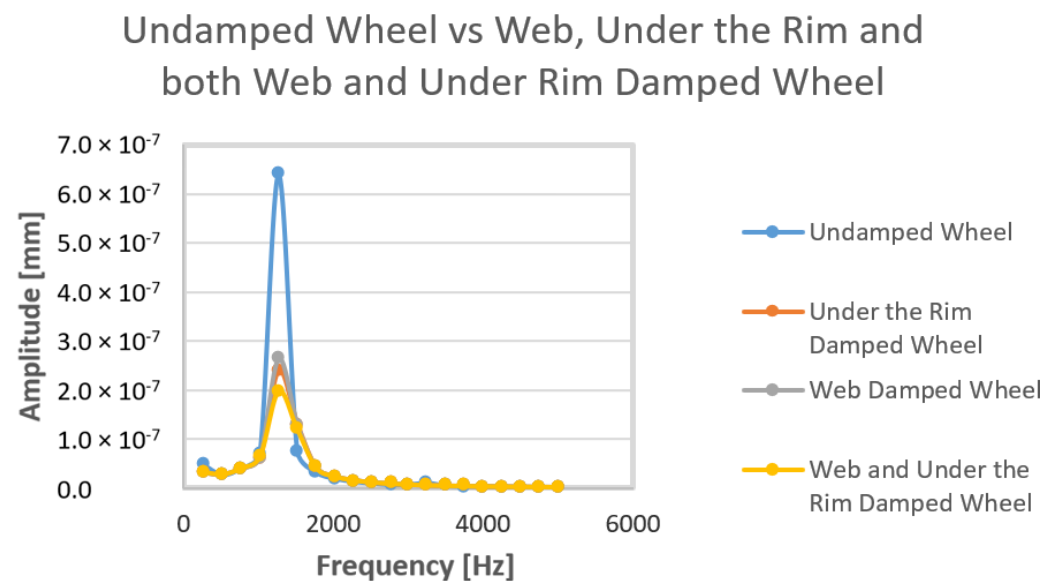
### 3.3.3. Radial Harmonic Analysis of a Wheel Mounted with Viscoelastic Layer on Both Sides of the Web and under the Rim

Figure 16 shows the difference between the wheel without viscoelastic layers (undamped wheel) and the wheel mounted with viscoelastic layers (damped wheel) on the web and under the rim on both sides of the wheel during radial excitation. Evident from Figure 16b is that the undamped wheel during excitation would experience a maximum amplitude of  $640.24 \times 10^{-9}$  mm at a frequency of 1265 Hz. After the viscoelastic damping was mounted, the results undoubtedly reveal that the maximum peak was completely reduced.



**Figure 16.** Harmonic response analysis in the radial direction with viscoelastic damping layer on both sides of the web and under the rim. (a) Radial harmonic excitation of the wheel mounted with viscoelastic layer on both sides of the web and under the rim. (b) Radial excitation results of the wheel without (black) and with (red) viscoelastic layer mounted on the web and under the rim on both sides of the wheel.

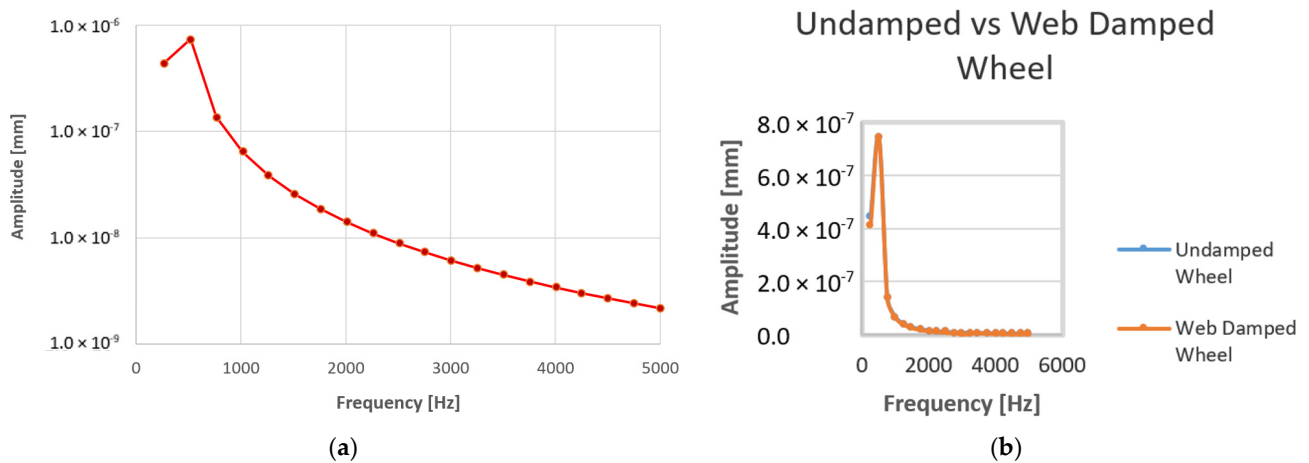
In Figure 17 was highlighted that the wheel, when mounted with a viscoelastic damping layer on both sides of the web and under the rim, would completely reduce the maximum amplitude resonance compared with when it was mounted with a viscoelastic damping layer on the web or under the rim during radial excitation.



**Figure 17.** Comparison between the undamped and damped (all arrangements) wheels.

### 3.3.4. Lateral Harmonic Analysis of a Wheel Mounted with Viscoelastic Layer on the Web of Both Sides of the Wheel

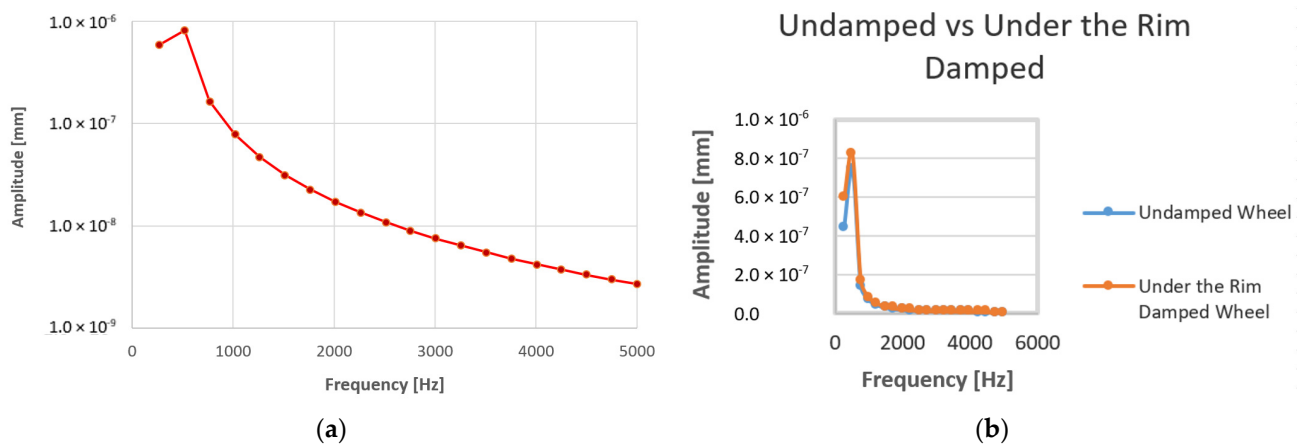
Figure 18 demonstrates the difference between the wheel without viscoelastic layer (undamped wheel) and the wheel mounted with viscoelastic layer on the web (damped wheel). The results from Figure 18b demonstrate that the undamped wheel during lateral excitation would experience a maximum amplitude peak of  $741.669 \times 10^{-9}$  mm at a frequency of 518 Hz. After the wheel was mounted with viscoelastic damping layer on the web and excited laterally, the wheel experienced a maximum amplitude of  $741.64 \times 10^{-9}$  mm at a frequency of 537 Hz.



**Figure 18.** Harmonic response analysis in the lateral direction with viscoelastic damping layer on the web on both sides of the wheel. (a) The lateral excitation results of the wheel with viscoelastic layer mounted on the web on both sides of the wheel. (b) The lateral excitation of the wheel without (black line) and with viscoelastic layer mounted on the web on both sides.

### 3.3.5. Lateral Harmonic Analysis of a Wheel Mounted with Viscoelastic Layer under the Rim on Both Sides of the Wheel

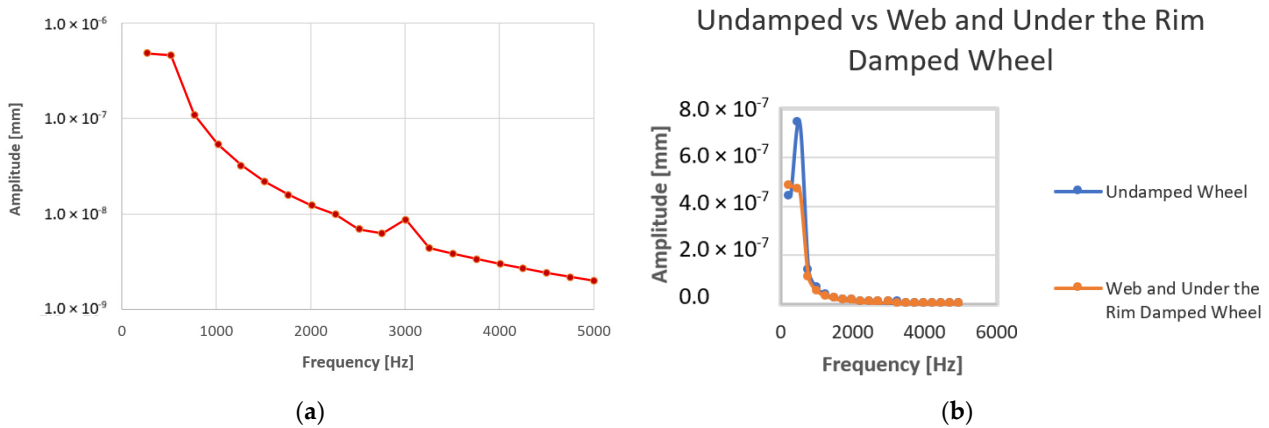
Figure 19b demonstrates the detailed analogy of the wheel without viscoelastic layer (undamped wheel) and with the wheel mounted with viscoelastic layer under the rim (damped wheel). The evidence from Figure 19b demonstrates that the undamped wheel would experience a maximum amplitude of  $741.669 \times 10^{-9}$  mm at a frequency of 518 Hz, while when the viscoelastic layer was mounted under the rim and excited laterally, the maximum amplitude the wheel experienced was  $817.35 \times 10^{-9}$  mm at a frequency of 518 Hz.



**Figure 19.** Harmonic response analysis in the lateral direction with viscoelastic damping layer under the rim of both sides of the wheel. (a) The lateral excitation on the wheel mounted with viscoelastic layer under the rim on both sides of the wheel. (b) Lateral results of the wheel mounted with and without viscoelastic layer under the rim on both sides of the wheel.

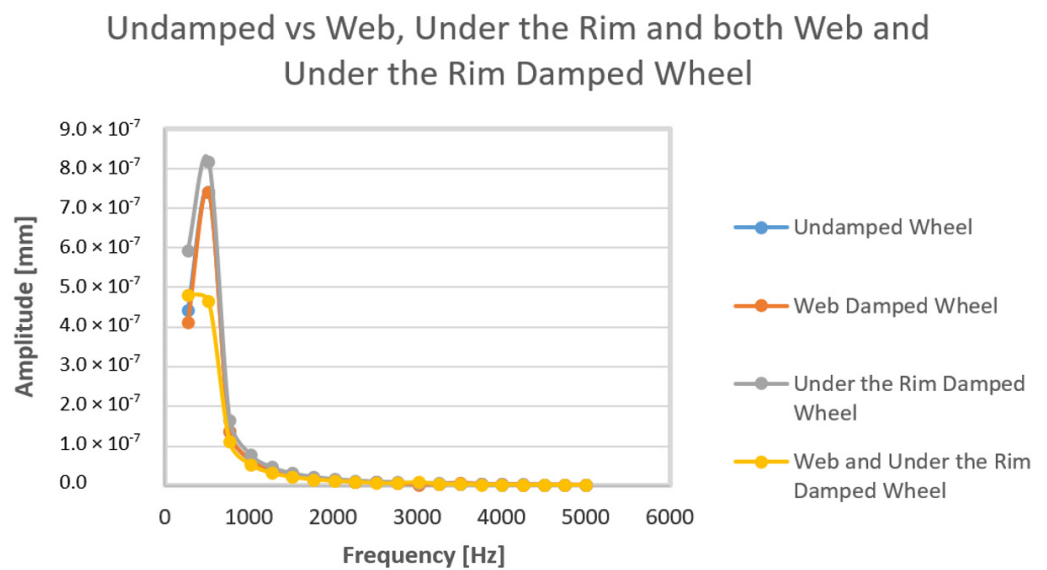
### 3.3.6. Lateral Harmonic Analysis of a Wheel Mounted with Viscoelastic Layer on the Web and under the Rim on Both Sides of the Wheel

Figure 20 demonstrates the detailed analogy of a wheel without viscoelastic layer (undamped wheel) and with a wheel mounted with viscoelastic layer on the web and under the rim (damped wheel). The evidence from Figure 20b demonstrates that the undamped wheel would experience a maximum amplitude of  $741.669 \times 10^{-8}$  mm at a frequency of 518 Hz, while when the viscoelastic layer was mounted under rim and excited laterally, the maximum amplitude the wheel experienced was  $465.166 \times 10^{-8}$  mm at a frequency of 518 Hz.



**Figure 20.** Harmonic response analysis in the lateral direction with viscoelastic damping layer under the rim on both sides of the wheel. (a) The lateral excitation on the wheel mounted with viscoelastic layer on the web and under the rim on both sides of the wheel. (b) Lateral results of the wheel mounted with and without viscoelastic layer under the rim on both sides.

Finally, Figure 21 shows the resonance peaks for lateral excitation for the three cases investigated. The evidence from Figure 21 proves that during lateral excitation, mounting the viscoelastic damping layer on both the web and under the rim on both sides of the wheel was more effective than when the viscoelastic damping layer was mounted under the rim on both sides of the wheel.



**Figure 21.** Comparison of the undamped wheel during lateral excitation with the web damped, the area under the rim damped and both the web and area under the rim damped at the same time.

#### 4. Discussion

In this section, some critical observations are presented to comprehensively understand the outputted results that were explored under the circumstances described above.

The results from Figures 12 and 17 show that the wheel experienced high amplitudes both from radial and lateral excitations. Hence, the frequency value, which was found to have a high amplitude peak on the wheel during excitation, was investigated as indicated in Table 7, which tabulates the natural frequencies and modal vibration numbers. It was found that the wheel resonance corresponded with the wheel mode vibration number 6 for lateral harmonic response and mode vibration number 10 for radial harmonic response. Based on these results, it can be concluded that the wheel would experience resonances at a frequency of 1265 Hz during radial excitation and 518 Hz during lateral excitation, because the harmonic responses of the wheel frequencies at resonance were equal to the natural frequencies of the wheel at mode vibration numbers 6 and 10, respectively.

After the viscoelastic damping layer was mounted in three different configurations on the wheel during radial excitation, the evidence from Figure 17 demonstrates that the viscoelastic damping layer, when mounted on the web and under the rim on both sides of the wheel, exhibited a better damping efficiency than the other cases. After the viscoelastic damping layer was mounted on the web and under the rim on both sides of the wheel, the maximum amplitude was found to be reduced by  $442.02 \times 10^{-9}$  mm. In the second configuration investigated, when the viscoelastic layer was mounted on the web on both sides of the wheel, the maximum amplitude peak at the resonance frequency was reduced by  $400.7 \times 10^{-9}$  mm. The final case investigated when the viscoelastic layer was mounted under the rim on both sides of the wheel, and it showed that the maximum amplitude peak at the resonance frequency was reduced by  $375.84 \times 10^{-9}$  mm. Furthermore, when the damping viscoelastic layer was mounted in three different cases on the wheel during lateral excitation, the evidence from Figure 21 demonstrates that the viscoelastic damping layer, when mounted on the web and under the rim on both sides of the wheel, exhibited a better damping efficiency than the other cases, because the undamped wheel's maximum amplitude peak was found to be reduced from  $741.669 \times 10^{-9}$  mm to  $465.14 \times 10^{-9}$  mm. That means that the layer was able to reduce the amplitudes by  $737.02 \times 10^{-5}$  mm from the vibrating peak value. In the second case (under lateral excitation), when the viscoelastic damping layer was mounted on the wheel web on both sides of the wheel, the maximum amplitude peak at the resonance frequency was reduced from  $741.669 \times 10^{-9}$  mm to  $741.64 \times 10^{-9}$  mm, indicating that the layer was able to reduce the amplitudes by  $290 \times 10^{-13}$  mm from the vibration peak value. In the last case (under lateral excitation), when the viscoelastic damping layer was mounted under the rim on both sides of the wheel, the maximum amplitude peak was not reduced, since it was found to increase from  $741.669 \times 10^{-9}$  mm to  $817.33 \times 10^{-9}$  mm. These findings have good agreement with the findings from Rizwan et al. [7], as they concluded that at certain points during excitation, the damping layer could not be effective on the structure. However, the technique shows good efficiency for suppressing both the radial (vertically) and lateral (horizontally) dynamics of the wheel, except during lateral excitation, when the viscoelastic layer was mounted on the web and under the rim.

Cervello et al. [16] used the same design procedure proposed in this paper to analyze and design a low-noise railway wheel but adopted a constrained damping layer treatment. Jones and Thompson [39] used a combination of finite element complex modal analysis and TWINS software Version 1.1 to calculate the mode shapes and modal masses of the wheel. The constrained damping layer was designed to mount the wheel with different configurations. It is clear that much work was performed to suppress rail wheel vibration using a constrained damping layer. In the present paper, a viscoelastic damping layer (unconstrained damping layer) was selected to reduce excessive vibrations on the locomotive wheel set.

It is clear from Table 7 that the mode shapes of the wheel's natural frequency during both radial and lateral excitations had an extensive impact on the wheel deformation. The

displacement of the wheel depended upon the change of direction and modal shape of the wheel.

It is clear from Figure 9b and Appendices A–C that the nodes of the wheel mounted with a viscoelastic layer on the web, under the rim and both on the web and under the rim were situated around the light blue color in the code legend. That correlated with the least displacement of the deformed shape and was dominating with respect to the average (yellow and green) and large (red) displacement. The only deformation taking place was on the viscoelastic damping layer, and it can be assumed that this occurred during flexure of the wheel, causing the viscoelastic damping layer to dissipate vibrations by means of compression and tension.

## 5. Conclusions

The mitigation of vibrations on locomotive wheels by using a numerical and experimental modeling method to design a viscoelastic mechanism was investigated in this manuscript. Three different arrangements were designed and analyzed to examine the effectiveness of the viscoelastic damping layers mounted at different positions in the locomotive wheel. The damping mechanism employed in the study showed good efficiency in suppressing both the radial (vertical) and lateral (horizontal) vibration dynamics of the wheel. The interesting findings deduced from this manuscript can be helpful to train wheel design engineers to mitigate rail wheel vibrations. The configurations from Figure 16 showed a better efficiency in reducing the maximum amplitude peaks than the configurations from Figures 14 and 15 during radial excitation. During lateral excitation, the configurations from Figure 18 demonstrated a better efficiency in mitigating the vibration modes than the configurations from Figures 20 and 21.

The results from Figure 12 clearly validate that the locomotive wheel experienced higher amplitude resonance peaks during lateral excitation than during radial excitation, in agreement with the findings from Balekwa and Kallon [9], when the wheelset of a D39 200 locomotive was excited using a hammer to investigate the vibrational resonance in the lateral, longitudinal and radial directions. Figures 17 and 21 give evidence for the viscoelastic damping layer to be a good damper to mitigate the resonance peaks of the wheel when properly mounted. Furthermore, the viscoelastic damping layer was revealed to be more effective under radial excitation than lateral excitation.

**Author Contributions:** M.P.: methodology, software, validation, formal analysis, investigation, data curation, writing—original draft, writing—review and editing and project administration; D.V.V.K.: conceptualization, methodology, validation, formal analysis, data curation, resources, writing—original draft and supervision; B.M.B.: formal analysis, methodology, investigation, data curation and writing—review and editing; M.C.: conceptualization, methodology, validation, formal analysis, data curation, resources, writing—review and editing and funding acquisition. All authors have read and agreed to the published version of the manuscript.

**Funding:** This research was supported by Università degli Studi di Catania within the CRUI-CARE Agreement (Research Path Starting Grant 2020-2022 Linea 3—Progetto NASCAR—Prot. 308811).

**Data Availability Statement:** Not applicable.

**Conflicts of Interest:** The authors declare no conflict of interest.

Appendix A

Table A1. Natural frequency and mode shapes for D39 200 locomotive wheel.

Mode Number	Frequency (Hz)	Mode Shapes	Classification and Descriptions
1	222.15		<p>Lateral Mode: It is noted that the wheel starts experiencing high deformation at the wheel flange and rim.</p>
2	223.61		<p>Lateral Mode: It is noted that only the wheel rim and flange will experience large stresses, which results in bending of the web.</p>
3	302.9		<p>Lateral Mode: Here, some bending of the web occurs. The wheel rim, flange and web experience larger deformations.</p>
4	459.92		<p>Lateral Mode: It is noted that the least deformed area is on the wheel hub, and the larger deformed area is on the wheel flange.</p>

Table A1. Cont.

Mode Number	Frequency (Hz)	Mode Shapes	Classification and Descriptions
5	460.91		<p>Radial Mode: It is clear that the cross-section of the wheel starts to alter when the axial bending commences.</p>
6	543.31		<p>Lateral Mode: The wheel flange and rim are laterally twisted, which may result in altering the web shape.</p>
7	1137		<p>Radial Mode: It is clear that the wheel experiences larger deformations on the rim, flange and under the rim, with the web affected the least. The wheel starts to exhibit axial bending in this mode.</p>

Table A1. Cont.

Mode Number	Frequency (Hz)	Mode Shapes	Classification and Descriptions
8	1137.2		<p>Radial Mode: It is clear from the cross-section that this is the onset of bending. The least affected area is on the wheel hub.</p>
9	1223.4		<p>Radial Mode: Here, the wheel mode shape changes further. It is noted that the whole wheel starts to distort.</p>
10	1224.7		<p>Radial Mode: It is noted that the most affected areas with larger deformations are on the flange, rim and under the rim.</p>

Table A1. Cont.

Mode Number	Frequency (Hz)	Mode Shapes	Classification and Descriptions
11	1769.6		<p>Radial Mode: It is clear that the mode shape is being dominated by bending in this cross-section, although the wheel web is not out of shape.</p>
12	1847.8		<p>Radial Mode: Axial bending is clearly noticed here. It is noted that larger displacements occur on the wheel rim.</p>
13	1848.5		<p>Lateral Mode: It is noted that the wheel web, rim and flange are out of their original shapes and are distorted.</p>

Table A1. Cont.

Mode Number	Frequency (Hz)	Mode Shapes	Classification and Descriptions
14	2032.7	<p>ANSYS 2021 R1 ACADEMIC  <b>A: Modal</b>                  Total Deformation 15                  Type: Total Deformation                  Frequency: 2032.7 Hz                  Unit: mm                  Deformation Scale Factor: 23 (Auto Scale)                  8/13/2021 10:15 AM</p> <p>3.3257 Max                  2.9581                  2.5896                  2.2171                  1.8476                  1.4781                  1.1086                  0.73904                  0.36952                  0 Min</p> <p>0.00 300.00 600.00 (mm)</p>	<p>Lateral Mode: It is noted that mode 14 is distorted further to reach this mode, with larger deformed areas on the wheel web, under the rim and on the rim and flange.</p>
15	2038.2	<p>ANSYS 2021 R1 ACADEMIC  <b>A: Modal</b>                  Total Deformation 16                  Type: Total Deformation                  Frequency: 2038.2 Hz                  Unit: mm                  Deformation Scale Factor: 23 (Auto Scale)                  8/13/2021 10:15 AM</p> <p>3.3215 Max                  2.9524                  2.5834                  2.2143                  1.8453                  1.4752                  1.1072                  0.7381                  0.36905                  0 Min</p> <p>0.00 300.00 600.00 (mm)</p>	<p>Radial Mode: It is noted that the wheel is dominated by bending in three different mode shapes and directions.</p>
16	2163.2	<p>ANSYS 2021 R1 ACADEMIC  <b>A: Modal</b>                  Total Deformation 17                  Type: Total Deformation                  Frequency: 2163.2 Hz                  Unit: mm                  Deformation Scale Factor: 20 (Auto Scale)                  8/13/2021 10:15 AM</p> <p>3.837 Max                  3.4107                  2.9843                  2.558                  2.1317                  1.7053                  1.279                  0.85266                  0.42633                  0 Min</p> <p>0.00 300.00 600.00 (mm)</p>	<p>Radial Mode: It is noted that the wheel from mode 16 bends further in this cross-section, although the wheel web is not out of shape. Only the entire wheel rim under the rim and flange shapes is distorted.</p>

Table A1. Cont.

Mode Number	Frequency (Hz)	Mode Shapes	Classification and Descriptions
16	2169.2		<p>Radial Mode: The mode shapes of the wheel start to recover from severe bending of modes 16 and 17.</p>
17	2575.4		<p>Lateral Mode: The mode shape of the wheel web is starting to deform. The mode shape of the wheel flange and the rim is fully recovered from the bending of mode numbers 16 and 17.</p>
18	2578		<p>Lateral Mode: It is clear that the mode shape of the wheel web and the hub are out of shape.</p>

Table A1. Cont.

Mode Number	Frequency (Hz)	Mode Shapes	Classification and Descriptions
19	2939		<p>Lateral Mode: The wheel web is twisted further, causing the wheel hub to shift out of its original position.</p>

**Appendix B. Mode Shapes for D39 200 Locomotive Wheel Vibration Mounted with Viscoelastic Damping Layer on the Web of Both Sides**

The legend in Figure A1 outlines the displacements with the units in millimeters. The color coding in the legend is matched with the colors in the deformed shape of the model results. It is noted that the nodes of the wheel situated around the light blue color of the deformed shape displaced the least. It can be deduced that after the viscoelastic layer is embedded in the wheel and is able to eliminate the red coding legends from the wheel, which represent high deformation. This implies that high deformation can be avoided by adding the viscoelastic damping layer on the wheel. Figure A1 shows the mode shapes of the wheel mounted with viscoelastic damping layer on the web of both sides when it starts to experience high amplitudes.

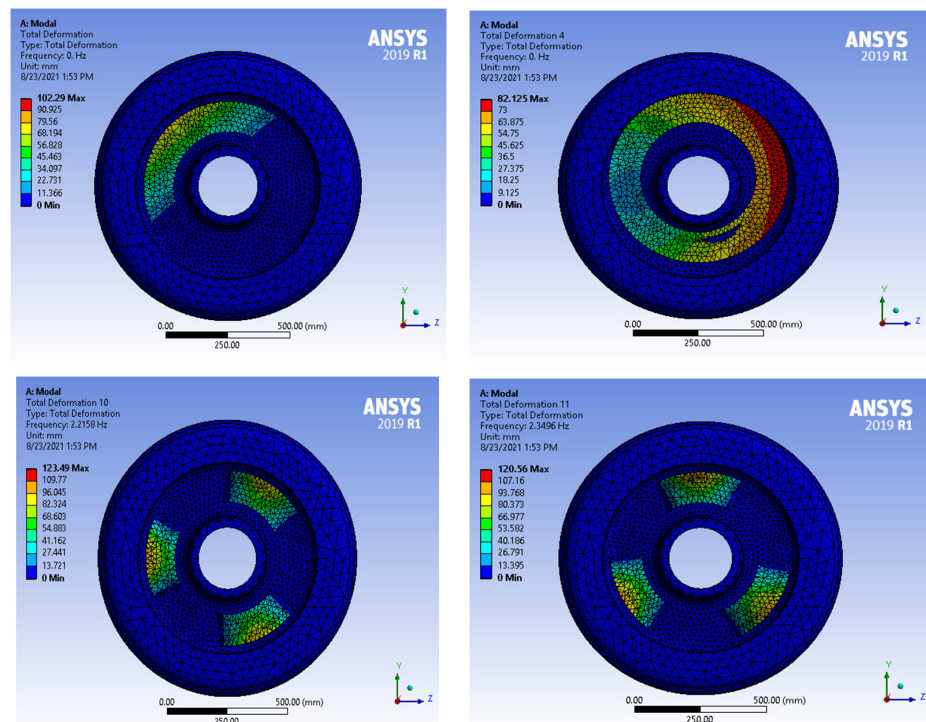


Figure A1. First four mode shapes of the wheel mounted with viscoelastic damping layer on the web.

**Appendix C. Mode Shapes for D39 200 Locomotive Wheel Vibration Mounted with Viscoelastic Damping Layer under the Rim of Both Sides**

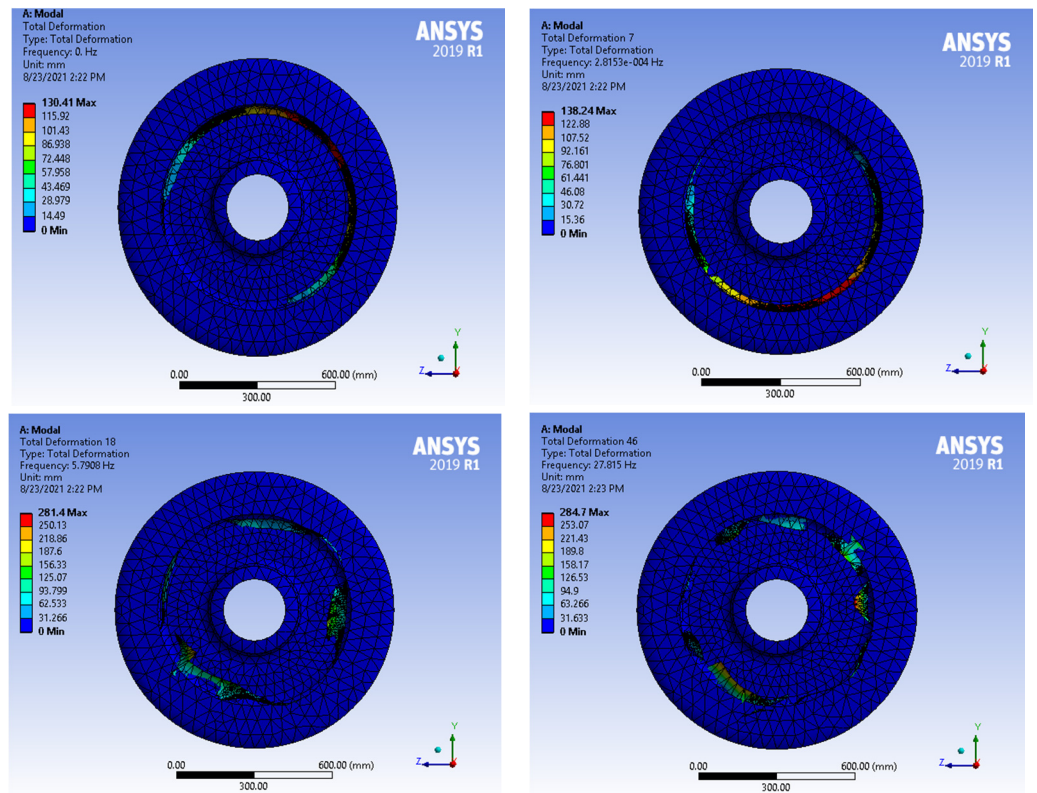


Figure A2. Mode shapes of the wheel mounted with viscoelastic damping layer under the rim of both sides when it starts to experience high amplitudes.

**Appendix D. Mode Shapes for D39 200 Locomotive Class Wheel Vibration Mounted with Viscoelastic Damping Layer on the Web and under the Rim of Both Sides**

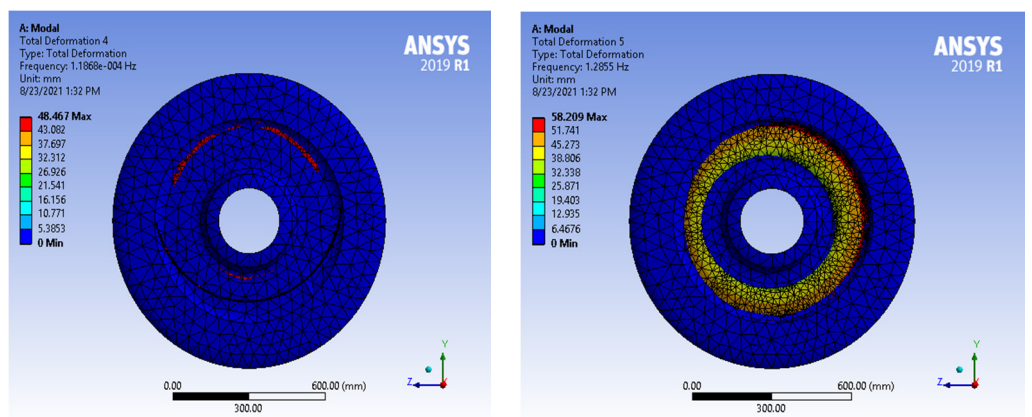
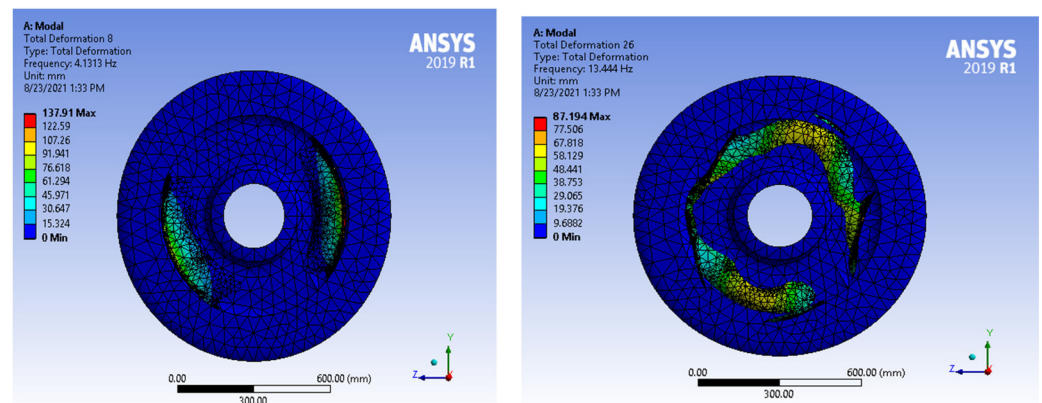


Figure A3. Cont.



**Figure A3.** Mode shapes of the wheel mounted with viscoelastic damping layer on the web and under the rim of both sides when it starts to experience high amplitudes.

The wheel with the viscoelastic damping layer situated around the light blue color code of the deformed shape displaced the least. It is clear that node 10 will experience less deformation compared with the wheel without the viscoelastic damping layer, since the light blue color dominates the color legends on the wheel.

**Appendix E. Scheme for Numerical Modal Analysis of a Wheel Mounted with and without Viscoelastic Layer**

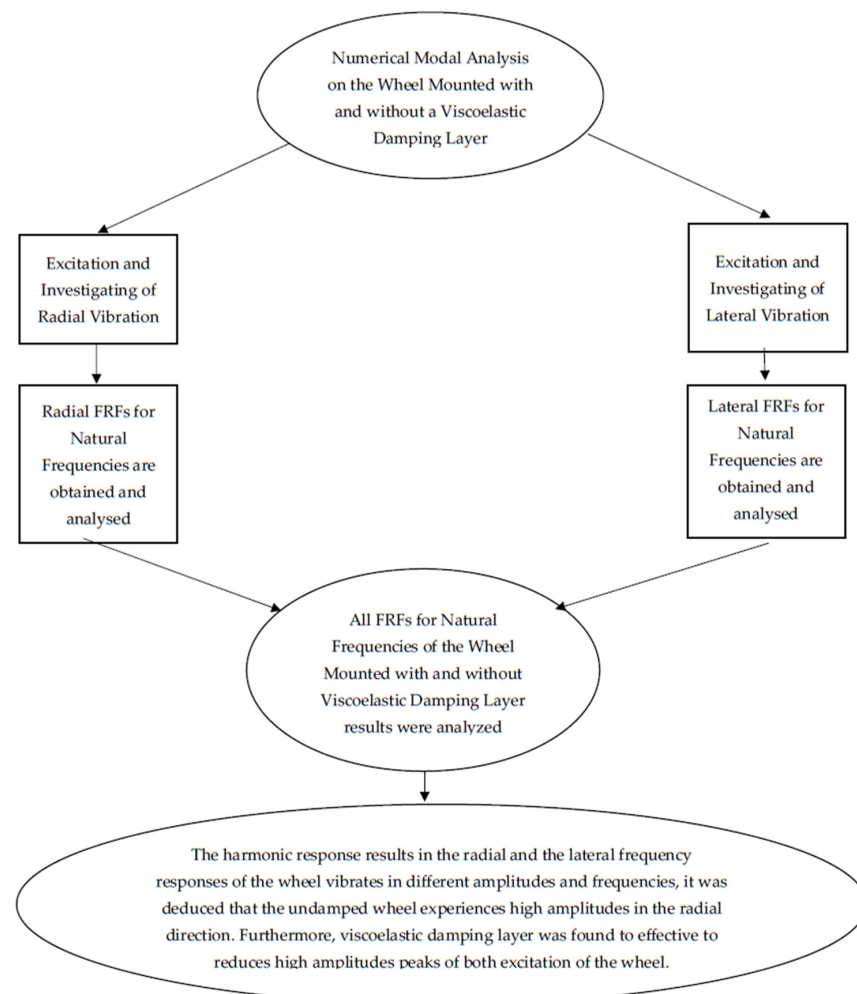


**Figure A4.** Experimental modal analysis scheme.

## References

1. Thompson, D.J. Wheel–rail noise generation, part I, II, III, IV and V. *J. Sound Vib.* **1993**, *161*, 387–482. [[CrossRef](#)]
2. Sato, K.; Sasakura, M.; Akutsu, K.; Sato, T.; Ishii, Y. Acoustic characteristics of wheels with different Web shapes. *Q. Rep. Railw. Tech. Res. Inst.* **2006**, *47*, 28–33. [[CrossRef](#)]
3. Zhong, T.; Chen, G.; Sheng, X.; Zhan, X.; Zhou, L.; Kai, J. Vibration and sound radiation of a rotating train wheel subject to a vertical harmonic wheel-rail force. *J. Mod. Transp.* **2008**, *26*, 81–95. [[CrossRef](#)]
4. Klrschner, F. New Developments in the Control of Railroad Wheel Screech Noise. In Proceedings of the INTER-NOISE and NOISE-CON Congress and Conference Proceedings, Reston, VA, USA, 1 January 1972.
5. Mazilu, T. On the structural vibration of the railway wheel. *Ann. Fac. Eng. Hunedoara* **2016**, *14*, 67.
6. Miller, H.M.; Incl, H. *Transit Noise and Vibration Impact Assessment*; Final Report; Federal Transit Administration: Washington, DC, USA, 2006; Chapter 7.
7. Rizwan, U.H.S.; Muhammed, I.S.; Jian, W.; Dong, Y.S. Effect of viscoelastic material thickness of damping treatment behavior on gearbox. *Res. J. Appl. Sci. Eng. Technol.* **2012**, *4*, 3130–3136.
8. Balekwa, B.; Kallon, D.; Mashamba, A.; Dube, P. Application of modal analysis to establish the wavelength fixing mechanism for rail corrugation. In Proceedings of the 11th South African Conference of Computational and Applied Mechanics, Vanderbijlpark, South Africa, 17–19 September 2019; pp. 212–223.
9. Balekwa, B.M.; Kallon, D.V.V. Correlation of short pitch corrugation with railway wheel-track resonance at low frequencies of excitation. *Vibration* **2020**, *3*, 491–520. [[CrossRef](#)]
10. Merideno, I.; Nieto, J.; Gil-Negrete, N.; Gil-Negrete, N.; Gimenez Ortiz, J.G.; Landaberea, A.; Iartza, J. Numerical characterization of railway wheels with sandwich-type damping solution. In Proceedings of the ISMA2014—International Conference on Noise and Vibration Engineering, Leuven, Belgium, 15–17 September 2014.
11. Balekwa, B.; Danie, F.; Kallon, D.V.V. Vertical and Horizontal Vibration Response for Corrugated Track Curves Supported on Steel and PY-Type Concrete Sleepers. In Proceedings of the 2019 Open Innovations Conference (OI), Cape Town, South Africa, 2–4 October 2019; pp. 474–482.
12. Balekwa, B.; Kallon, D.V.V. Vibration Response for class D44 and D39 200 Locomotive Wheelsets due to Dynamic Loads Excitation. In Proceedings of the 2019 Open Innovations Conference (OI), Cape Town, South Africa, 2–4 October 2019; pp. 418–421.
13. Thompson, D. *Railway Noise and Vibration: Mechanisms, Modelling, and Means of Control*; Elsevier: Oxford, UK, 2009.
14. Bangarubabu, K.; Kishre Kumar, K.; Krishna, Y. Damping effect of viscoelastic materials on sandwich beams. In Proceedings of the International Conference on Trends in Industrial and Mechanical Engineering (ICTIME2012), Bali, Indonesia, 30 June–1 July 2012.
15. Nashif, A.D.; Jones, D.I.G.; Henderson, J.P. *Vibration Damping*; John Wiley & Sons, Inc.: New York, NY, USA, 1985.
16. Cervello, S.; Donzella, G.; Pola, A.; Scepi, M. Analysis and Design of Low-Noise Railway Wheel. *J. Rail Rapid Transit* **2001**, *215*, 179–192. [[CrossRef](#)]
17. Lopez, I.; Vera, E.; Busturia, J.M.; Vinolas, J. Theoretical and experimental analysis of ring damped railway wheels. In Proceedings of the ISMA21 Conference, Leuven, Belgium, 18–20 September 1996; pp. 787–794.
18. Brunel, J.F.; Dufrénoy, P.; Charley, J. Analysis of the attenuation of railway squeal noise by preloaded rings inserted in wheels. *J. Acoust. Soc. Am.* **2010**, *127*, 1300–1306. [[CrossRef](#)]
19. Koizumi, S. Advance in railway vehicle technology and future prospectus mainly in relation to bogie. *Nippon Steel Sumitomo Met. Tech. Rep.* **2013**, *105*, 11–18.
20. Thompson, D.J.; Jones, C.J.C.; Waters, T.P.; Farrington, D.A. tuned damping device for reducing noise from railway track. *Appl. Acoust.* **2007**, *68*, 43–57. [[CrossRef](#)]
21. Kwon, H.C.; Kim, M.C.; Lee, I.W. Vibration control of bridges under moving loads. *Comput. Struct.* **1998**, *66*, 473–480. [[CrossRef](#)]
22. Samani, F.S.; Pelicano, F.; Masoumi, A. Performances of dynamic vibration absorbers for beams subjected to moving loads. *Nonlinear Dyn.* **2013**, *73*, 1065–1079. [[CrossRef](#)]
23. Chopra, A.K. *Dynamics of structures. Theory and Applications on Earth-Quake Engineering*, 4th ed.; Prentice Hall: Englewood Cliffs, NJ, USA, 2012.
24. Den Hartog, J.P. *Mechanical Vibrations*, 4th ed.; McGraw-Hill Book Company: New York, NY, USA, 1956.
25. Den Hartog, J.P. *Mechanical Vibrations*, 3rd ed.; McGraw-Hill Book Company: New York, NY, USA, 1947.
26. Rail-Wheel Vibration Absorber. Bochumer-Verein. Available online: <https://www.bochumer-verein.de/en/angebot/absorber/> (accessed on 10 March 2021).
27. Suarez, B.; Serrano, B.J.; Rodriguez, P.; Blanquer, J. Comparison of vibration and rolling noise emission of resilient and solid monobloc railway wheels in underground lines. In Proceedings of the 7th World Congress on Railway Research, Montreal, QC, Canada, 4–8 June 2006.
28. Resilient Wheels. Bochumer-Verein. Available online: <https://www.bochumer-verein.de/en/gummigefedertes-bvv-rad-dreiteilig/> (accessed on 19 February 2021).
29. 3M. *Scotchdamp Vibration Control Systems: Product Information and Performance Data*; 3M Industrial Tape and Specialties Division: St. Paul, MN, USA, 1993.
30. Vaseques, C.M.A.; Rodrigues, J.D. Viscoelastic damping technologies for structural acoustic control of railway wheels. In Proceedings of the 8<sup>o</sup> Congresso Nacional de Mecânica Experimental, Guimarães, Portugal, 21–23 April 2010.

31. Sasikumar, K.S. Vibrational control of beam with composite constrained layer treatment. *Int. J. Latest Eng. Technol.* **2015**, *5*, 176–183.
32. Athishay, D.A.; Chandrashekar, C.V. Dynamic analysis of plate with viscoelastic material patches. *Int. J. Technol. Res. Eng.* **2015**, *2*, 1038–1044.
33. Patil, V.; Talole, M.; Kharche, P.P.; Mahesh, M.S. Analysis of constrained layer treatment for damping in skin panels of aircraft. *Int. J. Trend Res. Dev.* **2016**, *3*, 313–317.
34. Cali, M.; Oliveri, S.M.; Ambu, R.; Fichera, G. An Integrated Approach to Characterize the Dynamic Behaviour of a Mechanical Chain Tensioner by Functional Tolerancing. *Stroj. Vestn. J. Mech. Eng.* **2018**, *64*, 245–257.
35. Jiang, Z.; Zhang, Z.; Hu, Y.; Sehneider, T.; Zorin, D.; Panozo, D. Bijective and coarse high-order tetrahedral meshes. *ACM Trans. Graph.* **2021**, *40*, 16. [[CrossRef](#)]
36. Kim, J.C.; Yun, Y.S.; Noh, H. Analysis of wheel of squeal and flanging on curved railway tracks. *Int. J. Precis. Eng. Manuf.* **2019**, *20*, 2077–2087. [[CrossRef](#)]
37. Nielsen, J.C.O.; Freso, C.R. Multi-disciplinary optimization of railway wheels. *J. Sound Vib.* **2006**, *293*, 510–521. [[CrossRef](#)]
38. Jones, C.J.C.; Thompson, D.J. Rolling noise generated by railway wheels with visco-elastic layers. *J. Sound Vib.* **2000**, *231*, 779–790. [[CrossRef](#)]
39. Pascon, J.P.; Coda, H.B. High-order tetrahedral finite elements applied to large deformation analysis of functionally graded rubber-like material. *Appl. Math. Model.* **2013**, *37*, 8757–8775. [[CrossRef](#)]
40. Fourie, D.J.; Gräbe, P.J.; Heyns, P.S.; Fröhling, R.D. Experimental characterization of railway wheel squeal occurring radius curves. *J. Rail Rapid Transit* **2016**, *230*, 1561–1574. [[CrossRef](#)]
41. Trindade, M.A.; Benjeddou, A. Hybrid active-passive damping treatments using viscoelastic and piezoelectric materials: Review and assessment. *J. Vib. Control* **2002**, *8*, 699–745. [[CrossRef](#)]
42. Moreira, R.; Rodrigues, J.D. The Modelisation of Constrained Damping Layer Treatments Using the Finite Element Method: Spatial Model and Viscoelastic Behavior. In Proceedings of the International Conference on Structural Damping Modelling, Test Analysis, Correlation and Validation, Madeira, Portugal, 3–5 June 2002; Available online: <https://repositorio-aberto.up.pt/bitstream/10216/69852/2/58299.pdf> (accessed on 10 December 2021).
43. Rahman, H.; Gupta, C. Computation of Rayleigh damping coefficient of rectangular submerged floating tunnel (SFT). *SN Appl. Sci.* **2020**, *2*, 936. [[CrossRef](#)]